# On modeling the diffusion to kinetically controlled burning limits of micron-sized aluminum particles

CrossMark

Brian T. Bojko [a], Paul E. DesJardin [a,*], Ephraim B. Washburn [b]

[a] Department of Mechanical and Aerospace Engineering, University at Buffalo, The State University of New York, Buffalo, NY 14260-4400, USA
[b] Naval Air Warfare Center Weapons Division, China Lake, California, USA

### ABSTRACT

Aluminum particle burn rates are known to be a strong function of particle size as the mode of burning transitions from diffusion to kinetically controlled. To better understand the rate dependent diffusion and kinetic processes, a fully compressible, one-dimensional, spherically symmetric particle burn model is developed. Several cases are studied to explore the burning of aluminum particles in air, carbon-dioxide and steam environments. Predictions of burn rates versus particle size reveal significant deviations from a diffusion controlled burning limit – highlighting the importance of accounting for finite-rate chemistry in modeling the burning of sub-micron aluminum particles. While overall agreement to data is satisfactory, the detailed model cannot be directly used in system level tools due to computational cost. Two reduced modeling strategies are therefore explored to account for finite-rate chemistry effects in simpler models for use in system level CFD analysis. The first is an augmented $D^2 - law$ where the finite-rate chemistry is treated as a perturbation to flame sheet approximation via augmented burn rate "constants". Predictions using this approach of deflagration speeds in dusty aluminum-air gases agree well with experiments and show evidence of a maximum flame speed for a given mass loading. The second modeling approach uses a reduced numerical model and kinetics mechanism resulting in computationally efficient solutions. Results using this approach show up to two orders of magnitude reduction in computational effort while maintaining reasonable accuracy for predictions of flame structure, burn rates and burn times.

## 1. Introduction

The use of aluminum particles continues to be of interest as an additive for propellants [1] and aviation fuels [2,3] to increase energy density and specific impulse. Recent studies have focused on the transition of diffusion to kinetically controlled burning with decreasing particle size [4–6]. One of the motivations for studying this transition is the potential of using sub-micron to nano-scale sized particles in fuels to shorten ignition times [7] and accelerate flame speeds [5].

The transition of diffusion to kinetically controlled combustion was studied by Bazyn et al. and Lynch et al. as a function of both particle size and pressure using a reflected shock-tube facility for $O_2$ and $CO_2$ environments [4,8]. For a pressure of 8.5 atm, the limit of a diffusion flame was observed to occur for particle sizes less than ~20 μm as reactions migrate closer to the droplet surface.

Aluminum particle combustion in the 2–20 μm range was studied by Badiola et al. by igniting particles generated using an electro-static aerosol generator and ignited with a $CO_2$ laser [9]. Using AlO emission measurements to determine burn times and average temperatures, Badiola et al. estimated the transition from diffusion to kinetically controlled combustion at ~10 μm in air.

Washburn et al. conducted detailed numerical simulations of aluminum particles in oxygen, carbon dioxide and steam environments [6,10]. Cases were conducted using 3–11 μm sized particles and compared to burn time data from Bazyn et al. [4,11]. Overall agreement was reasonable with some discrepancies observed for pressures below ~10 atm in $CO_2$ and $H_2O$ environments. Differences were attributed to the distribution of particles in the experiments which tends to skew burn time measurements at lower pressures.

Huang et al. conducted a study of flame speed of aluminum particle dust in air [5]. Model predictions of flame speed are compared to data using phenomenologically derived burn rate models. For larger micron-sized particles, ignition temperature is correlated with data and the overall mixture burn rate uses particle burn time

* Corresponding author.
    E-mail address: ped3@buffalo.edu (P.E. DesJardin).

**Nomenclature**

| | | | | |
|---|---|---|---|---|
| $D$ | mass diffusivity (m$^2$/s) | | $Z$ | mixture fraction |
| $D_p$ | particle diameter (m) | | | |
| $e_t$ | total energy (J/kg) | | *Greek* | |
| $H_t$ | total enthalpy (J/kg) | | $\alpha$ | thermal diffusivity (m$^2$/s) |
| $h^o_{f,i}$ | heat of formation of species $i$ (J/kg) | | $\gamma$ | constituent density (kg/m$^3$) |
| $h_{vap}$ | latent heat of vaporization of aluminum (J/kg) | | $v$ | mass based stoichiometric ratio |
| $K$ | burn rate constant (m$^2$/s) | | $\rho$ | mixture density (kg/m$^3$) |
| $\dot{m}_i$ | mass flow rate (kg/s) | | $\rho_{air}$ | density of ambient air (kg/m$^3$) |
| $\dot{m}_i'''$ | mass source term of species $i$ (kg/m$^3$ s) | | $\rho_u$ | density of unburnt mixture (kg/m$^3$) |
| $\dot{m}_F'''$ | mass consumption rate of fuel (kg/m$^3$ s) | | $\varphi$ | constituent volume fraction |
| $m_o$ | initial mass of the particle (kg) | | $\Phi$ | equivalence ratio |
| $m_q$ | mass of quenched particle (kg) | | | |
| $\dot{m}_T$ | bulk mass flow rate in radial coordinates (kg/s) | | *Subscripts/superscripts* | |
| $r$ | radial coordinate (m) | | $i$ | $i$th species |
| $\dot{S}$ | flow rate of species towards the surface (kg/s) | | $l$ | liquid property |
| $S_L$ | flame speed (m/s) | | $q$ | quenching limit |
| $\tau_b$ | burn time (s) | | $s$ | particle surface |
| $T$ | temperature (K) | | $T$ | total property |
| $Y_i$ | species mass fraction | | $\infty$ | ambient/far-field conditions |

correlations developed by Beckstead [12]. For smaller nano-sized particles, the burn rates are assumed to follow that of a molecular limit using the chemical kinetics mechanism developed by Catoire et al. [13]. Flame speed predictions are shown to scale with decreasing particle diameter as $\sim d^{-0.92}$, consistent with $D^2$ theory (see discussion regarding estimates of $S_L$ in results section). For particles less than $\sim 10\ \mu$m, however, further reduction in particle diameter results in a more gradual increase in flame speed, scaling as $\sim d^{-0.52}$, as the rate of burning becomes more kinetically controlled. Huang et al. estimate a maximum flame speed of 5.82 m/s as the particle diameter reaches a molecular asymptotic limit.

The transition from diffusion to kinetically controlled combustion is a recurring theme in the aforementioned studies and plays a crucial role in burning modes for decreasing pressures and particle sizes. In particular, particles that are $\sim 10\ \mu$m and smaller exhibit a clear dependence on the rate limiting chemical kinetics. Relations between the Damköhler and Knudsen numbers have been made to help describe the mode of combustion of particles [14], but to date there have not been theoretical estimates of this transition as a function of particle size for aluminum particles, although estimates have been made for other energetic materials [15,16]. Typically, considerations of such a transition have been studied through the correlation of burn times versus pressure which exhibits a transition when pressure decreases and burn times increase. If pressure is held constant, burn rates will be a function of particle diameter and asymptotically approach a converged, diffusion-controlled burn rate as particle size increases.

Although experimentally derived empirical burn time relations have been developed to account for the burning behavior of aluminum particles for different burning regimes [17,8,18,9], they are limited to the select conditions of the experiment where the far-field temperature, pressure and oxidizer are held constant during the burning process. In system level applications using aluminum particulate (*e.g.*, a rocker motor) the far-field conditions will most likely not remain constant. Detailed CFD models such as those by Washburn et al. [6,10] and Gallier et al. [19] do account for varying far-field conditions, however they are far too complex for use with system level simulations of multiphase flows involving billions of particles. An alternative description is therefore desirable which can balance complexity with accuracy of burn rates as the particle transitions from diffusion to kinetically controlled limits. Exploring

modeling strategies which can accommodate these constraints is a focus of this study.

The rest of the study is as follows. A fully compressible, one-dimensional, spherically symmetric model formulation is first presented that accounts for the full chemistry, differential diffusion, *etc.* using kinetic theory of gases. The purpose of the detailed model is to serve as the "exact" solution for which reduced approaches can be compared against. Validation is conducted using the experimental data and simulations of Bucher et al. [20] and also to measurements of Bazyn et al. [4] and numerical simulations of Washburn et al. [6] which span the diffusion to kinetically controlled burning transition regime. Two reduced modeling approaches are explored. The first relies on couching burn rates in terms of a modified $D^2$-law where a normalized burn rate "constant" ($K$) becomes a function of particle diameter and pressure to account for the effects of finite-rate chemistry. The normalized burn rate constants can be combined with eigenvalue based analytical solutions of the flame structure to account for effects of finite-rate chemistry. This model is used to compute flame deflagration speeds of aluminum-air dusty gases and compared to theory and data. The second reduced model is a simplified numerical model that employs quasi-steady assumption of mass transfer and reduced kinetics allowing for an efficient fully implicit formulation. Flame structure comparisons are presented using this model compared to the more general fully compressible formulation and errors in burn rates and flame structure are characterized.

## 2. Detailed model

The starting point for a detailed model is a spherically symmetric particle. The particle is assumed to have been heated sufficiently such that the aluminum oxide shell has fractured and collected on the particle surface to form the alumina cap. Assuming the Biot number is much less than unity, the aluminum particle in the molten liquid phase has a uniform temperature throughout. Since the focus of this study is not to explore multi-dimensional effects, a spherically symmetric configuration is the simplest geometry that needs to be considered for studying diffusion to kinetically controlled burning. The multiphase gas flow is considered one-dimensional, fully compressible and viscous resulting in the following set of transport equations for mass, species, momentum and energy conservation.

$$\frac{\partial(\rho r^2)}{\partial t} + \frac{\partial(\rho u r^2)}{\partial r} = 0 \tag{1a}$$

$$\frac{\partial(\rho Y_i r^2)}{\partial t} + \frac{\partial(\rho u Y_i r^2)}{\partial r} = \frac{\partial}{\partial r}\left(r^2 \rho D_i \frac{\partial Y_i}{\partial r}\right) + \dot{m}_i''' r^2 \tag{1b}$$

$$\frac{\partial(\rho u r^2)}{\partial t} + \frac{\partial(\rho u^2 r^2)}{\partial r} = -r^2 \frac{\partial p}{\partial r} + \frac{\partial}{\partial r}\left[r^2 \mu \left(2\frac{\partial u}{\partial r} - \frac{2}{3}(\frac{\partial u}{\partial r} + u/r)\right)\right] \tag{1c}$$

$$\frac{\partial(\rho e_t r^2)}{\partial t} + \frac{\partial(\rho u H_t r^2)}{\partial r} = \frac{\partial}{\partial r}\left[r^2 u \mu \left(2\frac{\partial u}{\partial r} - \frac{2}{3}\left(\frac{\partial u}{\partial r} + u/r\right)\right)\right]$$
$$+ \frac{\partial}{\partial r}\left[r^2 \left(k\frac{\partial T}{\partial r} + \sum_i^N \rho D_i \frac{\partial Y_i}{\partial r} h_i\right)\right] - r^2 \sum_i^N \dot{m}_i''' h_{f,i}^o \tag{1d}$$

where $e_t(= e + u_r^2/2)$ is the total sensible energy, $H_t(= e_t + p/\rho)$ is the total enthalpy and $u$ is the radial component of velocity. CHEM-KIN formatted reaction mechanisms and transport properties (i.e. $C_P$, $k$, $D_{i-j}$, etc.), are tabulated for each temperature and pressure between 300 K and 5000 K; and 0.5 atm and 30 atm for efficient lookup during run-time. Mixing rules of Mathur et al. [21] and Bird et al. [22] are used to determine mixture weighted diffusion ($D_i$) and thermal conductivity ($k$), respectively. Soret and Dufor diffusion effects are neglected. A locally homogenous flow (LHF) approximation is employed to account for the alumina condensate where the diffusion coefficient of alumina is set to be the lowest of the gas-phase constituents, consistent with previous studies [19]. The density in Eq. (1) represents the mixture density of solid and gas phases, $\rho = \gamma_s \varphi_s + \gamma_g \varphi_g$, where $\gamma$ and $\varphi$ are the density and volume fraction for each phase. The density of solid phase alumina is assumed to be a constant, $\gamma_s = 3950$ kg/m$^3$. Consistent with the LHF approximation, pressure and thermal equilibrium is assumed to exist between the solid and gas phases.

The aluminum oxidization mechanism used by Washburn et al. [10,6] is employed in this study and summarized in Appendix A. This mechanism consists of 46 reaction steps and 22 species for oxidation in $O_2$, $CO_2$ and $H_2O$ environments. Although new reaction pathways have recently been considered for aluminum-steam environments by Starik et al. [23], they have not been included in the current mechanism. Heterogeneous surface reactions for aluminum particle combustion should be of importance when considering a kinetically controlled combustion regime, however a kinetic mechanism to describe such a process does not currently exist and therefore is omitted from the current study. It is assumed that condensation reactions occur in the gaseous phase and migrate to the surface of the particle to form the alumina cap. This assumption provides an upper limit on the amount of alumina that can be deposited to the surface and has shown to provide reliable estimates of deposition rates in previous studies [24]. Other mechanisms have been postulated for the deposition of alumina onto the particle surface, such as the entrainment of metal oxide particles into a recirculation zone on the leeward side of the particle [25]. Such mechanisms are not considered in the present study. All other species are assumed insoluble in liquid aluminum and therefore mass fluxes are set equal to zero at the surface. The heat transfer into the liquid is neglected, employing an isothermal assumption. The resulting boundary conditions at the particle surface are as follows,

mass: $\dot{m}_T = \dot{m}_{Al} - \dot{S}_{Al_2O_3}$ \hfill (2a)

aluminum: $\dot{m}_{Al,l} = \dot{m}_T Y_{Al,s} - 4\pi r_s^2 \rho D_{Al} \frac{dY_{Al}}{dr}\Big|_s$ \hfill (2b)

alumina: $-\dot{S}_{Al_2O_3} = -4\pi r_s^2 \rho D_{Al_2O_3} \frac{dY_{Al_2O_3}}{dr}\Big|_s$ \hfill (2c)

other species: $0 = \dot{m}_T Y_{i,s} - 4\pi r_s^2 \rho D_i \frac{dY_i}{dr}\Big|_s$ \hfill (2d)

energy: $\dot{m}_{Al,l} h_{vap} = 4\pi r_s^2 k_g \frac{dT}{dr}\Big|_s$ \hfill (2e)

the total mass flow rate is the difference between the evaporation of Al and deposition of $Al_2O_3$, where $\dot{S}_{Al_2O_3}$ is the rate of alumina deposition to the particle surface. Assuming saturation conditions at the liquid–vapor interface, the partial pressure of the aluminum vapor is related to the surface temperature ($T_s$) using a vapor pressure curve from Hultgren et al. $P_{Al,s} = exp[36.547 - 39033/T_s - 1.3981 \ln(T_s) + 6.7839 \times 10^{-9} T_s^2]$ [26].

A finite volume method is used to solve the coupled system of non-linear equations given in Eq. (1) using the surface boundary condition of Eq. (2) and defining the far-field conditions for all species, temperature and pressure. A second-order fractional step method is used to integrate the equations using a two-stage Runge–Kutta time integration. In this approach, source terms are constructed for processes of convection, diffusions and reactions. Convective fluxes are discretized using an AUSM + UP flux vector splitting [27] using a combination of second-order upwind biased and essentially non-oscillatory (ENO) interpolants for determining fluxes [28,29]. Molecular fluxes are approximated using second-order centered differencing employing a semi-implicit operator to avoid diffusion time step stability limitations. Chemical reactions are advanced for each RK stage using a semi-implicit RK solver with adaptive time step control. The equations are marched in time until a steady-state solution is achieved for determining burning rates and flame structure.

A critical aspect of the burning process of aluminum is the condensation and volatilization of the alumina. This phase change is primarily responsible for the increase in thermal energy when the condensate is formed. Liang and Beckstead developed a two-stage alumina condensation model using homogeneous nucleation theory along with an empirical set of constants which are tuned using experimental data [12]. A simpler approach is pursued here where the aluminum oxide is assumed to be in local phase-equilibrium with the surroundings. Although thermodynamic data is not available from empirical studies for alumina in its gaseous state, experimental observations of alumina vapor in plasma have been made by Desai et al. [30]. To determine the equilibrium concentrations, thermodynamic properties of gaseous $Al_2O_3$ are used from Swihart and Catoire [31] based on their ab initio molecular orbital calculations. Figure 1a shows representative predictions of Al, $O_2$, AlO, $Al_2O$, $Al_2O_3$, O and mixture temperature using this approach as a function of mixture enthalpy. These results are in good agreement with the estimates of Glassman shown in Fig. 1b and experimental work done by Lynch et al. [32] on the volatilization temperature of alumina and supports the concept of a limiting temperature associated with the dissociation of $Al_2O_3$ condensate.

As discussed recently by Ermoline et al., non-continuum effects should be considered when particle diameter is on the same order as the mean free path [33]. In their study, a zirconium–oxygen system was investigated. To understand if this limit is important in the present study, the evaporation rate of the aluminum is compared to the maximum evaporation predicted by the Hertz–Knudsen equation [34] which defines the maximum evaporation rate of a material in a vacuum. In the continuum limit, the evaporation of a single aluminum droplet may be estimated as: $\dot{m} = 2\pi D_p \rho D_{Al-air} \ln(1 - Y_{Al,s})$, where $D_{Al-air}$ is the binary diffusion coefficient (determined using Chapman–Enskog description of binary mixtures). Assuming saturation conditions at the particle surface, $Y_{Al,s} = (MW_{Al}/MW_{air})(P_{Al,s}/P)/(1 - P_{Al}/P + MW_{Al}/MW_{Air})$. The theoretical maximum evaporation rate for an aluminum droplet is given by the Hertz–Knudsen equation: $\dot{m} = \pi D_p^2 P_{Al,s}/\sqrt{2\pi R_{Al}T}$, corresponding to the evaporation of aluminum in a vacuum. Equating the two expressions for $\dot{m}$ and solving for $D_p$ provides an estimate of a critical diameter for which non-continuum effects start to play a role,

$$D_{p,crit} = \frac{-2\rho D_{Al-air} \ln(1 - Y_{Al,s})\sqrt{2\pi R_{Al}T_s}}{P_{Al,s}} \tag{3}$$
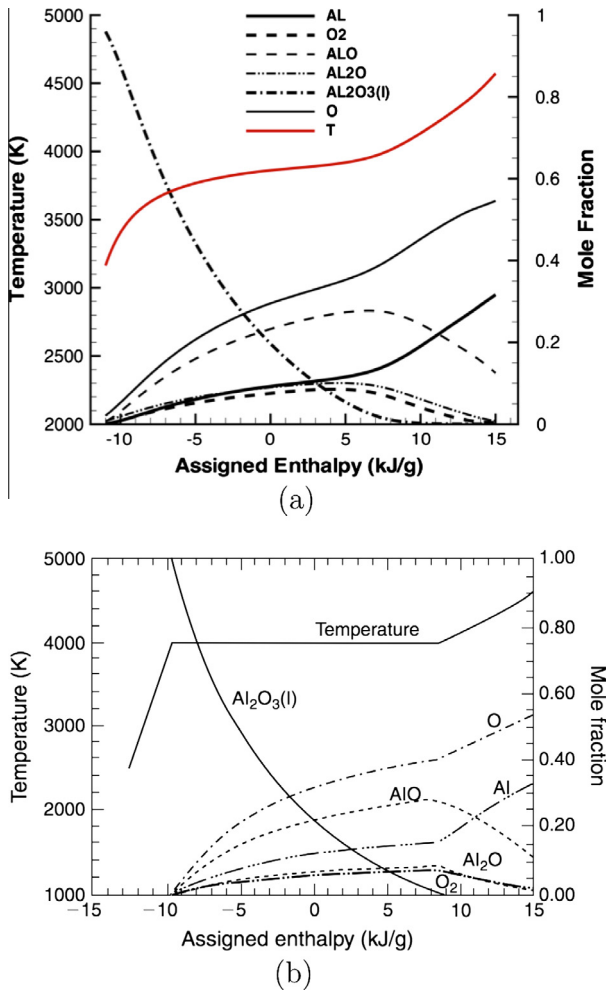
**Fig. 1.** Stoichiometric equilibrium calculations of current mechanism (a) as compared to equilibrium calculations considering the dissociation of alumina by Glassman [48] (b).

effects in the modeling, such as the introduction of a Knudsen layer [33]. With increasing temperature and decreasing pressure, the critical diameter increases. Non-continuum effects would therefore need to be introduced into the modeling for small particles at low pressures and at high temperatures. As will be discussed, the exact value of $T_s$ is a function of the particle size, oxidizer and far-field temperature and pressure, however, in the diffusion controlled burning limit, $T_s$ is independent of particle size and equal to 2625, 3306, 3519 and 3620 K for $P$ = 1, 10, 22 and 30 atm, respectively. For these cases, the corresponding values of critical diameter are $D_{p,crit} = 4.7, 0.91, 0.37$ and $0.27 \ \mu m$ and are shown in Fig. 2 with symbols. Continuum level modeling is applicable for particles larger than these sizes which is the case for all particle sizes consider in this study, with the exception of the 3 μm particle. However, it will be shown that as the 3 μm particle becomes kinetically limited at low pressures then $T_s$ falls below the diffusion mode limit, therefore the $D_{crit}$ criterion is still satisfied allowing for a continuum description of droplet burning.

## 3. Results and discussion

### 3.1. Flame shape

To validate the detailed model, 220 μm particle diameter cases are first conducted and compared to flame structure measurements of Bucher et al. [35]. To the author's knowledge, the data of Bucher et al. continues to serve as the sole source of flame structure data for aluminum combustion and is an excellent resource for model validation. Figure 3 shows comparisons of normalized mass fractions of AlO and Al₂O₃ along with temperature. Overall agreement to data is excellent with comparisons of AlO, matching the data within 10% error. The peak mass fraction of Al₂O₃ and the predicted profile also agrees well with the data. Remaining differences may be due in part to differences in chemical mechanism and diffusion models used for the alumina condensate.

### 3.2. Transitional burning modes via burn time correlations

Decreasing particle size results in a lower flame temperature and a migration of the flame to the surface. During this transition, the overall rate of burning passes from a diffusion to kinetically controlled process. This may be readily shown theoretically by

and is a function of temperature and pressure. Figure 2 presents $D_{p,crit}$ versus temperature for pressures of 1, 10, 22 and 30 atm. Particles with diameters below $D_{crit}$ would require non-continuum
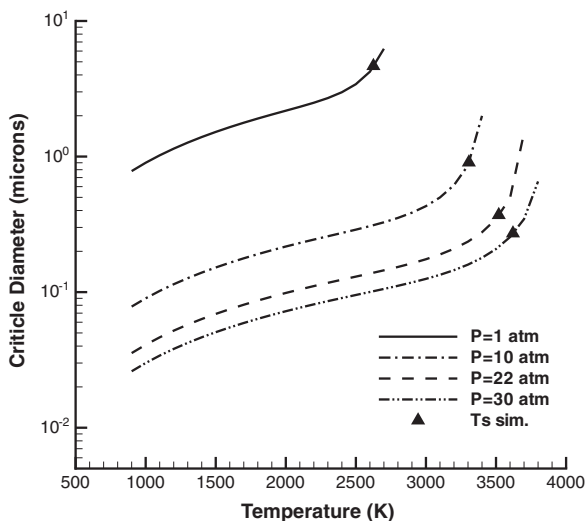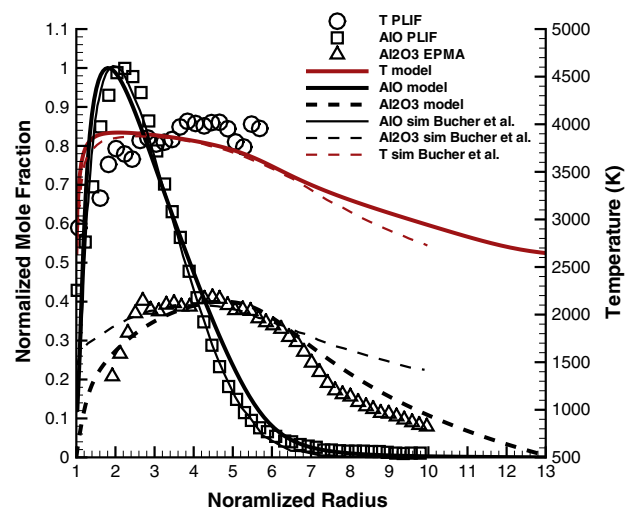


**Fig. 2.** Critical diameter versus temperature for pressures of 1, 10, 22 and 30 atm. The symbols mark the calculated surface temperature from the combustion simulations in the diffusion limit.



**Fig. 3.** Comparisons of temperature, AlO and Al₂O₃ predictions for a 220 μm particle with atmospheric conditions $T$ = 2650 K, in air at $P$ = 1 atm compared to data and simulations of Bucher et al. [35,20].

considering the limit of steady burning and mapping the species conservation equation in terms of mixture fraction, $Z$ (assuming constant diffusivity, $D$, for all species). In this limit, the overall mass flow rate ($\dot{m} = 4\pi\rho u r^2$) is constant, therefore Eq. (1b) becomes $d^2Y_i/dZ^2 = 2\dot{m}_i'''/(\rho\chi)$ where $\chi$ is the scalar dissipation rate. Solving the mixture fraction equation in spherical coordinates $\chi$ may be derived analytically, $\chi \equiv 2D[(\dot{m}Z - \dot{m}_Z)/(4\pi\rho D r^2)]^2$. In this expression, $\dot{m}_Z$ is the overall flow rate of mixture fraction and is a constant for steady burning. Near the flame at $Z = Z_{st}$, $\chi_{st}$ is proportional to $1/r^4$, indicating the fuel loading into the flame is a strong function of particle size. As the particle radius decreases, $\chi$ rapidly increases, reducing the effective chemical reaction rates. A reduction in the conversion rates results in the transition of burning from diffusion to kinetics controlled. From this analysis, it is reasonable to assume that all burning droplets will transition from diffusion to kinetically controlled modes of burning. The importance of the kinetically controlled burning regime of a droplet is therefore a function of what fraction of the total burning time is dominated by kinetic effects. For aluminum particles, this transitional size appears to be approximately 10 μm but is also strongly dependent on pressure through its effect on the diffusion coefficient.

To explore the transitional burning regime of aluminum particles, the experimental data of Bazyn et al. [4,11], Lynch et al. [8], and detailed numerical simulations of Washburn et al. [10,6] are used for comparison purposes. The experiments report burn times of aluminum in Ar-oxidizer mixtures with varying pressures where burn times are estimated using light emission collected from photo-diodes. For this comparison, burn times are computed as,

$$\tau_b = \int_{m_q}^{m_o} \frac{dm}{\dot{m}_{Al}} \qquad (4)$$

where $m_o$ and $m_q$ are the initial and quenched masses, respectively. $m_q$ is determined by systematically reducing the initial mass until a meaningful steady burning solution can no longer be found, *i.e.*, when the steady-state temperature throughout the computational domain does not rise above the far-field temperature and $Al_2O_3$ is not formed. Figures 4–6 show comparisons of burn times with varying (a) pressure and (b) far-field oxidizer using $O_2$, $CO_2$ and $H_2O$, respectively. Changes in the resulting flame structure are summarized in Figs. 7 and 8, showing flame structure at low and high pressures for $O_2$.

For the $O_2$ cases in Fig. 4, a smooth increase in burn times with decreasing pressure is observed as the mode of burning transitions from diffusion to kinetically controlled, resulting in lower burn rates. Within the uncertainty of the data, good agreement is observed between the detailed model predictions and the data. The detailed model predictions are consistently lower than those from Washburn et al. due to differences in the calculation of burn times. In Washburn et al., burn times are computed assuming $m_q = 0$, leading to larger values of $\tau_b$. Changes in the burn rates during this transition can be understood by comparing changes in the flame structure at low pressure (Fig. 7) versus high pressure (Fig. 8). At high pressure, the flame stand-off is slightly larger and peak flame temperature is 10% higher. The flame temperature and formation of $Al_2O_3$ is largely controlled by the transport of three species, Al, AlO and $Al_2O$. Distribution of the minor species is shown in Fig. 8b for the high pressure case. Al from the surface diffuses to the flame and forms AlO on the fuel rich side of the flame. The AlO formed in the flame diffuses back to the surface forming $Al_2O$. $Al_2O$, in turn, diffuses back to the flame, undergoing further oxidation to ultimately form $Al_2O_3$.

The rate of $Al_2O_3$ formation and peak temperature is therefore limited by the concentration of $Al_2O$ at the particle surface. At high pressures, the mass fraction of $Al_2O$ at the surface is 0.6 (Fig. 8b)
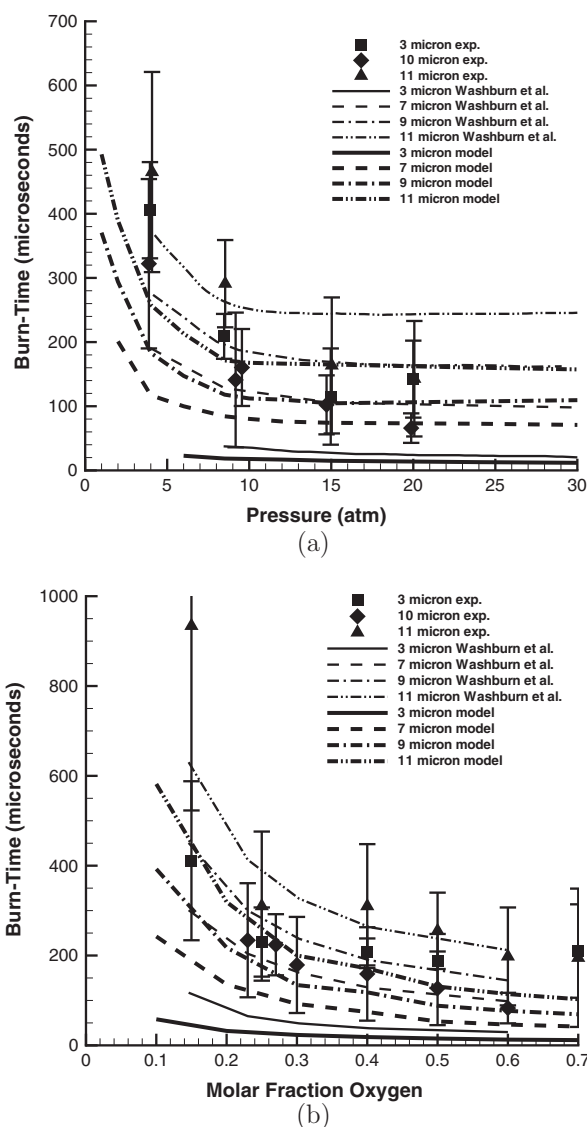


**Fig. 4.** Burn time comparisons with (a) varying pressure at $T = 2650$ K, 40% $O_2$ and 60% Ar and (b) varying $O_2$ for $P = 8.5$ atm, $T = 2650$ K.

compared to 0.18 at lower pressures (Fig. 7b). A higher concentration results in a higher mass loading of $Al_2O$ into the flame to form $Al_2O_3$. The concentration of $Al_2O$ at the surface, however, is a function of how quickly AlO is converted to $Al_2O$ near the particle surface. At high pressures all of the AlO is consumed at the particle surface (Fig. 8b) therefore the rate of burning is diffusion controlled by the diffusion of $Al_2O$. Decreasing the pressure within the high pressure regime ($P > 10$ atm) does not alter the flame structure much since the concentration of AlO at the flame surface remains zero. At low pressures, however, the mass fraction of AlO starts to grow, reaching 30% of its peak value for the $P = 4$ atm case shown in Fig. 7b. Subsequently, $Al_2O$ near the particle surface decreases, reducing the fuel loading rate into the flame. In this limit the burn rate is therefore ultimately controlled by the rate for which AlO forms $Al_2O$ near the particle surface, *i.e.*, a kinetically controlled process.

To further illustrate the trade-off between near-surface reactions and diffusion, Fig. 9 shows the Damköhler number versus normalized radius. The Damköhler number is defined as the ratio of the diffusion time scale of $Al_2O$ ($\tau_D$) to the chemical time scale ($\tau_C$) associated with the $AlO + Al \rightarrow Al_2O$ reaction rate. The
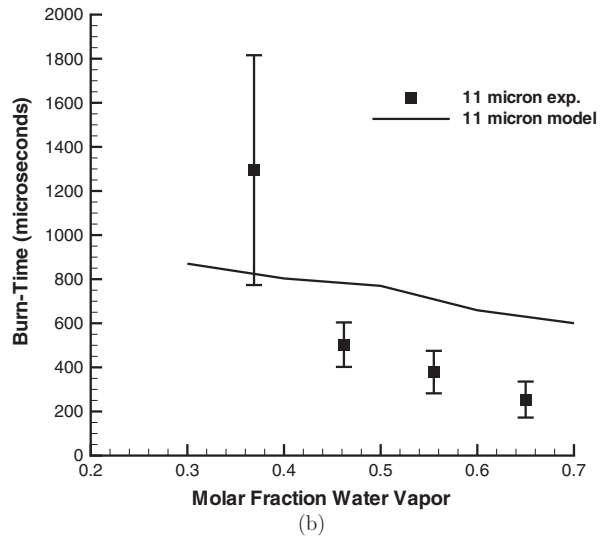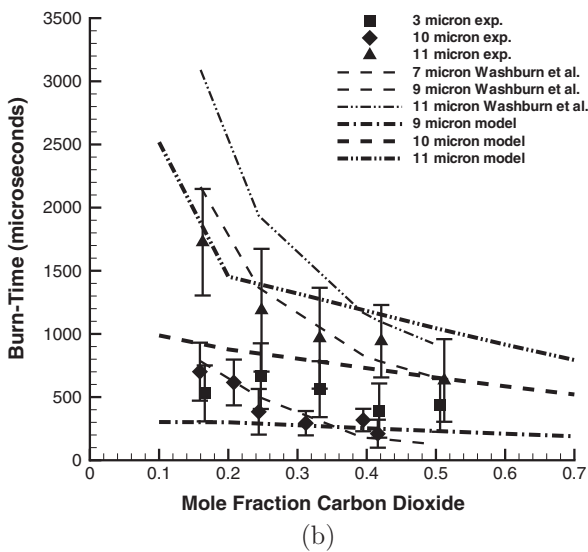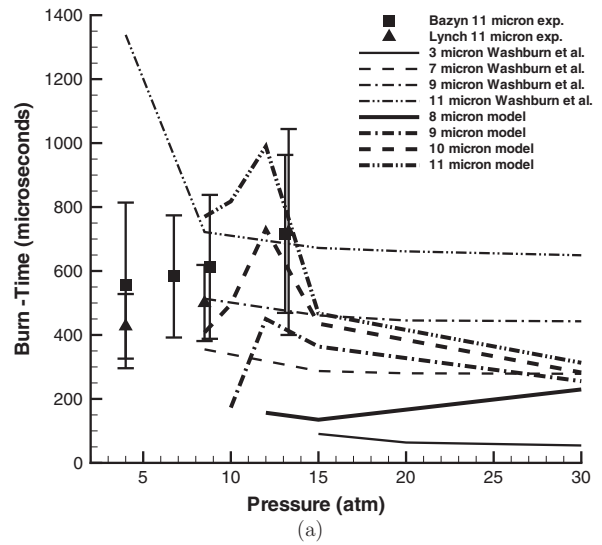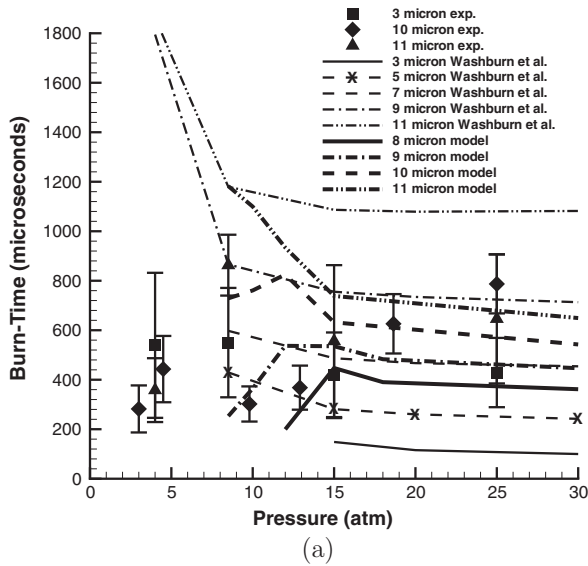
**Fig. 5.** Burn time comparisons with (a) varying pressure at $T = 2650$ K, 40% $CO_2$ and 60% Ar and (b) varying $CO_2$ for $P = 8.5$ atm, $T = 2650$ K.



**Fig. 6.** Burn time comparisons with varying pressure at $T = 2650$ K, 50% $H_2O$ and 50% Ar and (b) varying $H_2O$ for $P = 8.5$ atm, $T = 2650$ K.

diffusion time scale is determined as: $\tau_D = r^2/D_{Al_2O}$ where $D_{Al_2O}$ is the diffusivity of $Al_2O$. The chemical reaction time scale is determined as: $\tau_C = \rho/\dot{m}_i'''$, where $\dot{m}_i'''$ is either for the consumption of AlO or the production of $Al_2O$. At high pressures, $Da_{AlO} = -20$ and $Da_{Al_2O} = 27$ near the surface, indicating the production rate of $Al_2O$ is fast relative to diffusion, resulting in a high concentration of $Al_2O$ near the surface and hence a high mass flux loading of $Al_2O$ to the flame. At low pressures, the magnitude of $Da_{AlO}$ and $Da_{Al_2O}$ approach unity, lowering the concentration of $Al_2O$ near the surface since it is kinetically controlled – hence lowering the mass flux loading into the flame.

For burning in $CO_2$ and $H_2O$, the competition between the rate of diffusion of $Al_2O$ from the particle surface and the rate of AlO conversion is complicated by the possibility of flame quenching. Burn time versus pressure trends for $CO_2$ and $H_2O$ are shown in Figs. 5 and 6, respectively. The measurements show burn times are relatively constant for $CO_2$ and a slight downward trend is observed with increasing pressure for $H_2O$. Clearly, these cases are quite different from the $O_2$ runs. Earlier predictions by Washburn et al. (reproduced in Figs. 5 and 6) show a dramatic departure from the data, indicating increasing burn times with decreasing

pressure. The current detailed model showed trends similar to the earlier predictions of Washburn, if $m_q$ was set to zero. Using the augmented definition of burn times that includes $m_q$, however, the burn times are more in line with the data showing a downward trend at lower pressures. It should be pointed out, however, that the current simulations do not yield meaningful solutions at pressures lower than 8.5 atm for $CO_2$ and $H_2O$, where burn time measurements are reported. The reasons for these differences are potentially threefold. The first, is the experiments employed a distribution of particles whereas the model uses a single diameter. Conceivably the emission being monitored from the experiment could therefore be from burning particles in the upper end of the distribution that are not necessarily indicative of the mean particle size. Secondly, the emission may not represent steady burning since the particles are shock ignited. In the simulations, unsteady particle burning can be achieved using an elevated initial temperature, however the particle will eventually quench due to excessive heat loss to the surroundings. Thirdly, the model currently does not include heterogeneous surface reactions since they are not available and potentially will play a role in continued burning at low pressures by introducing an adsorption catalysis via C and H atoms to increase surface energy and promote combustion reactions [36].
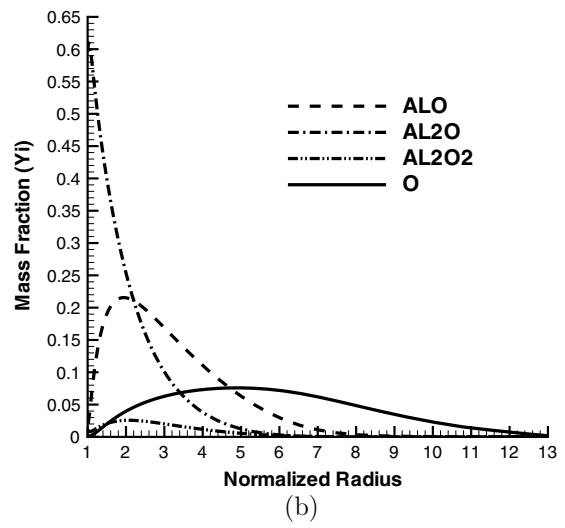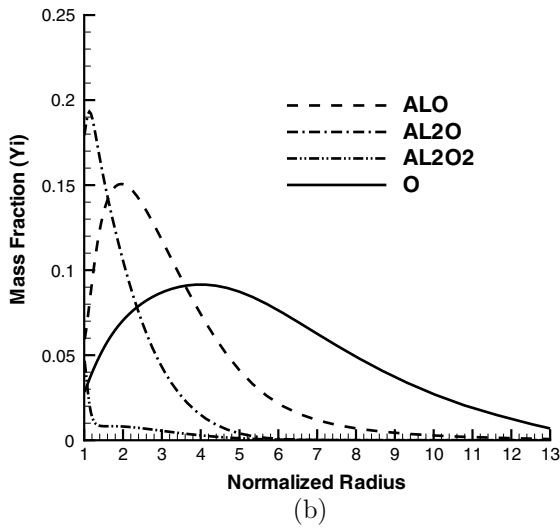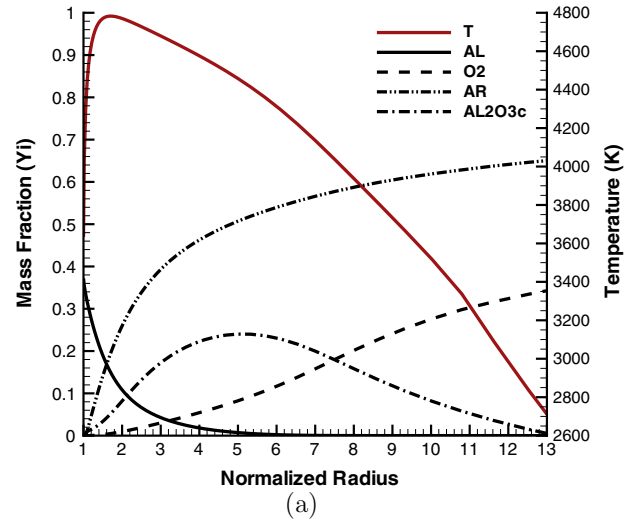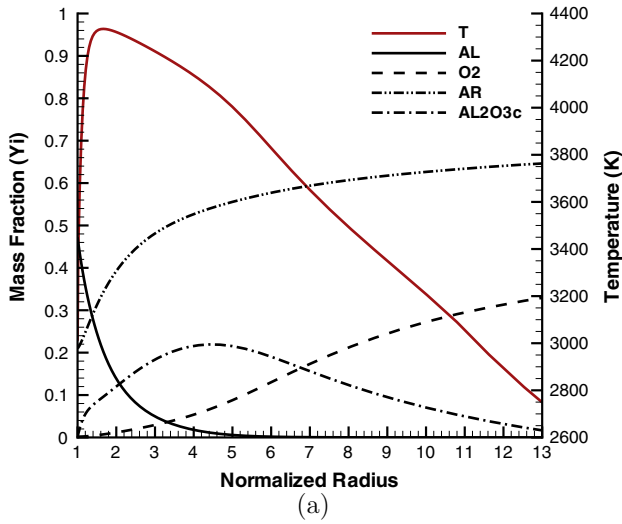
**Fig. 7.** Flame structure for major species and temperature (a) and minor species (b), for an 11 μm particle at atmospheric conditions $P = 4$ atm, $T = 2650$ K and 40% $O_2$ in Ar.



**Fig. 8.** Flame structure for major species and temperature (a) and minor species (b), for an 11 μm particle at atmospheric conditions $P = 30$ atm, $T = 2650$ K and 40% $O_2$ in Ar.

Despite these uncertainties, changes in AlO and $Al_2O$ near the surface in low versus high pressures for $CO_2$ and $H_2O$ are remarkably similar to those of $O_2$, highlighting the dominance of the AlO and $Al_2O$ pathways for defining the transition from diffusion to kinetically controlled burning.

### 3.3. Consequences for simplified particle modeling descriptions

Based on detailed simulations, it is clear that effects of finite-rate chemistry must be taken into account in simplified models of aluminum particle burning. While several simplified modeling approaches have been developed for engineering estimates of particle burn times and burn rates of aluminum particles, none can account for the diffusion to kinetically controlled burning transitions. Such a model is necessary for system level simulations of multiphase flows in the context of a subgrid scale (SGS) modeling for large eddy simulations [37,38].

The simplest particle modeling approach are burn time correlations derived using experimental data [17,8]. Beckstead provides an excellent review on many of these prior to 2005, many taken from the Russian literature [17]. Based on a large body of data, Beckstead estimated burn times to be, $\tau_b = aD^n / X_{eff} P^{0.1} T^{0.2}$ where
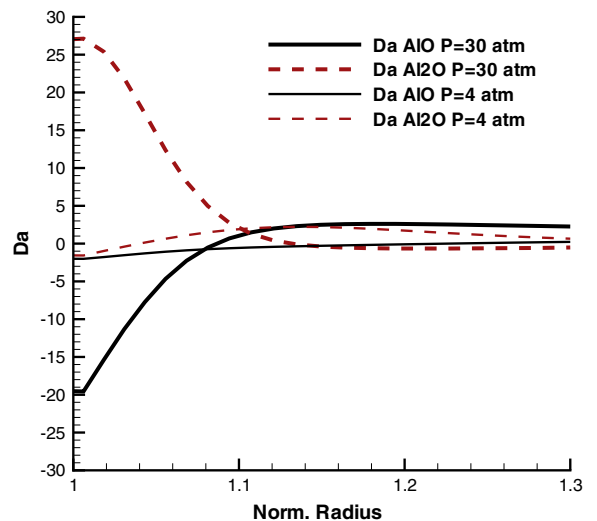


**Fig. 9.** Damköhler numbers versus normalized radius at low ($P = 4$ atm) and high ($P = 30$ atm) pressures.

$X_{eff}$ is the effective oxidizer concentration (for a mixture of $O_2$, $H_2O$ and $CO_2$) and $a$, $n$ are curve-fit constants. This correlation works well in the diffusion limited burning regimes. More recently, Lynch et al. [8] and Dreizin et al. [18,9] provided burn time corrections to account for the transitional burning regime. These correlations are very useful for when the "far-field" oxidizer, pressure and temperatures for the particle are fixed, e.g., an isolated burning particle in an environment with uniform composition and temperature. For many practical applications, flows are often turbulent and therefore the far-field conditions will change throughout the particle life-time. Burn rates are therefore more useful from a modeling perspective than burn times.

In the limit of diffusion controlled burning, simplified solutions for the gas-phase system can be developed using Schvab–Zeldovich coupling functions [24] or thin-flame zonal-analysis [1]. Changes in burn rates from far-field temperature, pressure and oxidizer composition can readily be computed and integrated with large-scale turbulent flow simulations [38]. These models, however, implicitly assume the mode of burning is diffusion controlled and therefore cannot account for the reduction in burn rates with decreasing particle size and pressure. As an illustration, Fig. 10 shows normalized burn rate "constant" ($K/K_{Max}$) versus diameter at different pressures for (a) $O_2$, (b) $CO_2$ and (c) $H_2O$, respectively. In the limit of large particles and high pressures, $K$ is truly a constant because the particle burns in a diffusion controlled mode, consistent with $D^2$ theory. $K_{max}(T, Ox)$ corresponds to the large particle/pressure limit when $K$ is a constant and may be readily computed using simplified descriptions of the flame structure. A decrease in $K/K_{max}$ from unity indicates particle burning transition from diffusion to kinetically controlled. In principle, these augmented $K/K_{max}(T, Ox, P, D)$ curves could be used with simplified $D^2$-type models. In this approach $K_{max}(T, Ox)$ is determined from the $D^2$-type model and corrected by tabulated values of $K/K_{max}$ as a function of pressure and diameter. As an example, predictions of flame speed of aluminum dusty gases are explored over a wide range of particle sizes and pressures. Predictions are compared to the detailed simulations of Huang et al. [5] and experimental data of Boichuk et al. [39], Goroshin et al. [40,41], Ballal [42] and Cassel [43] using simplified flame speed theory, $S_L = \left[ -2\alpha(v+1)\overline{\overline{\dot{m}}}'''_F / \rho_u \right]^{1/2}$; where $\alpha$ is the thermal diffusivity, $v$ is the mass based stoichiometric fuel to air ratio, $\overline{\overline{\dot{m}}}'''_F$ is the mass consumption rate of the fuel in the mixture and $\rho_u$ is the density of the unburned mixture [44]. Substituting in for $\overline{\overline{\dot{m}}}'''_F = n_d \dot{m} = (3\rho_{air}\Phi K)/(2vD^2)$, where $n_d$ is the particle density and $\dot{m}$ is the mass loss rate of the particle. The flame speed can be expressed as [45,46]:

$$S_L = \left[ \frac{3\alpha(v+1)\rho_{air}}{\rho_u} \frac{\Phi K}{v + \Phi} \right]^{1/2} \frac{1}{D}. \tag{5}$$

where $\Phi$ is the mixture equivalence ratio. In general, $K = K(T, Ox, P, D)$ can be re-expressed as: $K = K_{max}(K/K_{max})$ where $K/K_{max}$ comes from detailed simulations and $K_{max}(T, Ox)$ is determined using the reduced model developed by DesJardin et al. [24] which employs Schvab–Zeldovich coupling functions to determine the gas-phase solution, assuming diffusion controlled burning. For constant values of $K$, Eq. (5) shows that $S_L$ is inversely proportional to diameter, which is consistent with the findings of Huang et al. where a $D^{-0.92}$ power law was determined in the limit of large particles [5]. Decreasing particle sizes therefore results in an increase in flame speed from the associated increase in surface area. For small particles that are kinetically controlled, $K$ deceases, resulting in a maximum in flame speed as a function of diameter. Figure 11 shows this behavior with comparisons of predictions using Eq. (5) to data [5,39–43] and the limiting cases of kinetically and diffusion controlled burning modes, where $S_L$ scales as $D^{-0.52}$ and $D^{-1}$,
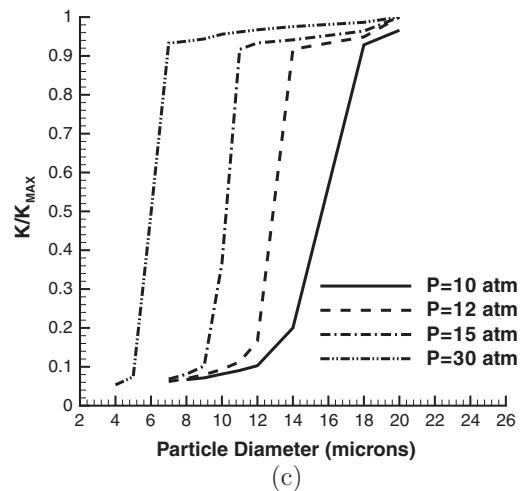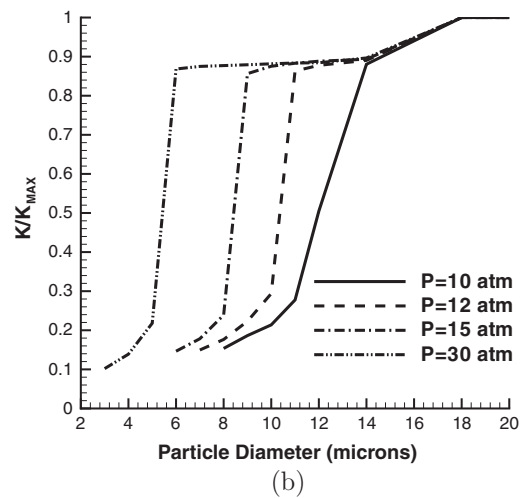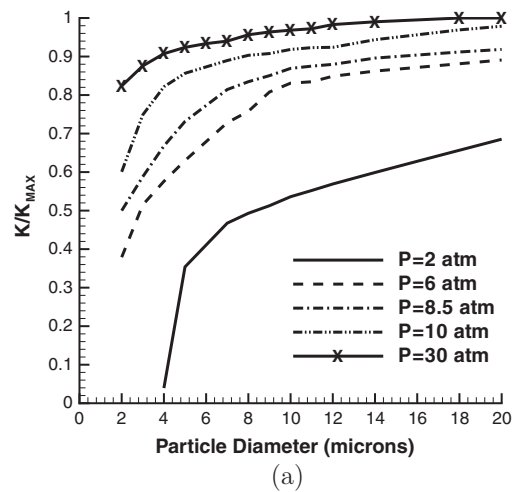


Fig. 10. Normalized $K$ versus particle diameter up to 20 μm for atmospheric conditions $T = 2650$ K at various pressures for (a) 40% $O_2$, (b) 40% $CO_2$ and (c) 50% $H_2O$.

respectively. Based on experimental burn time data, Huang et al. derived a $D^{-0.13}$ dependence which is also included in Fig. 11. Good agreement is shown between model predictions, data and scaling theories considering the simplified description of flame propagation given by Eq. (5).

While an augmented $D^2$ burn rate description is useful, it requires the creation of $K/K_{max}$ tables over a range of particle
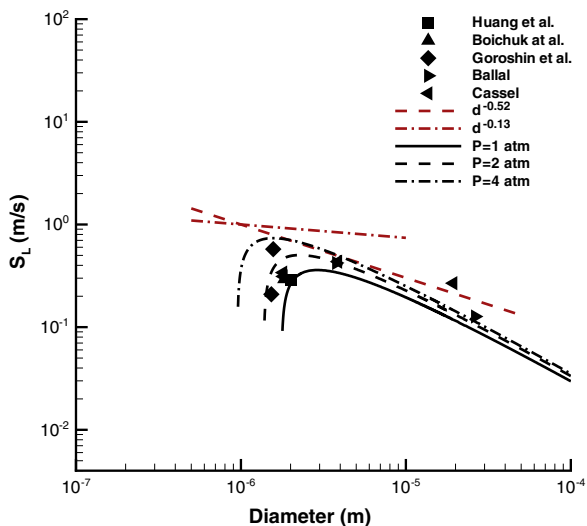
**Fig. 11.** Flame speed for aluminum particles in air with, $\Phi = 0.85$, $T_\infty = 300$ K compared to shock tube experimental data. Experimental data from Huang et al. [5], Boichuk et al. [39], Goroshin et al. [40,41], Ballal [42] and Cassel [43].



**Fig. 12.** Comparisons of a reduced mechanism and number of grid points for a 220 μm particle with atmospheric conditions $T = 2650$ K, in air at $P = 1$ atm as previously done.

diameters and pressures. It is therefore desirable to directly incorporate the finite-rate chemistry into a reduced model. More generalized coupling functions can be defined to solve the gas-phase system which do include finite-rate chemistry and have been developed largely for coal combustion [15,16]. While useful, these approaches are cumbersome to formulate with complex chemistry, *i.e.*, more than a single gas-phase reaction, since multiple species (more than 2) are needed to uniquely define coupling functions. Moreover, numerical int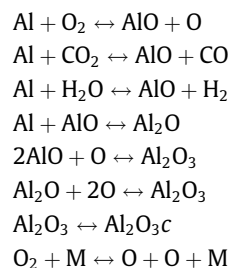egration of the energy equation is still required to obtain a solution. An alternative approach is therefore explored where Eq. (1) is greatly reduced by assuming: (1) gas is quasi-steady ($\dot{m} = 4\pi\rho u r^2$ is a constant), (2) equal diffusivities, (3) unity Lewis number and (4) neglecting pressure and viscous effects in momentum and energy. In this limit, transport of species and enthalpy can be expressed as:

$$\frac{\partial(\rho\beta r^2)}{\partial t} = \frac{\partial}{\partial r}\left(r^2\Gamma\frac{\partial\beta}{\partial r} - \beta\frac{\dot{m}}{4\pi}\right) + r^2\dot{S} \qquad (6)$$

where $\beta = \{Y_i, h\}$, $\Gamma = \{\rho D_m, k/C_P\}$ and $\dot{S} = \{\dot{m}_i''', -\sum_i^N \dot{m}_i''' h_{f,i}^o\}$. This system of equations is efficiently integrated to steady-state using a fully implicit fractional step method. The result is an order of magnitude less computational effort to solve the general equations given in Eq. (1) since the acoustic time scales of the problem have been removed. Furthermore, based on the findings from the detailed simulations, it is clear that the dominant species governing the diffusion to kinetically controlled burning transition are Al, AlO, and $Al_2O$. These observations lead to a reduction of the original 46 reactions from the full mechanism to a reduced set of 8 dominant reaction pathways.

$$Al + O_2 \leftrightarrow AlO + O$$
$$Al + CO_2 \leftrightarrow AlO + CO$$
$$Al + H_2O \leftrightarrow AlO + H_2$$
$$Al + AlO \leftrightarrow Al_2O$$
$$2AlO + O \leftrightarrow Al_2O_3$$
$$Al_2O + 2O \leftrightarrow Al_2O_3$$
$$Al_2O_3 \leftrightarrow Al_2O_3c$$
$$O_2 + M \leftrightarrow O + O + M$$

The rate constants for these reactions are the same as that for the full mechanism. While a more systematic chemical kinetic reduction
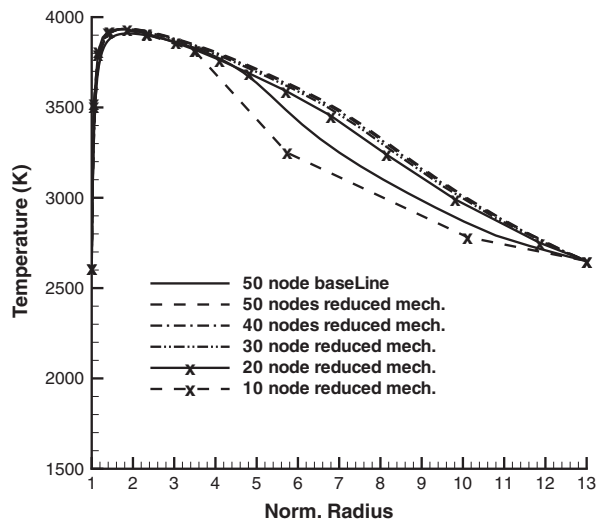
**Table 1**
Speedup comparisons using phenomenologically based reduced mechanism and quasi-steady formulation. The baseline case is fully compressible formulation using 50 nodes. All cases solved consider the burning of a 220 μm particle burning in air shown in Fig. 3.

| Nodes | Speedup | Burn rate (mm²/s) | % error |
|---|---|---|---|
| *Baseline* | 1.0 | 0.4918 | – |
| 50 | 7.0275 | 0.4461 | 9.30 |
| 40 | 22.165 | 0.4392 | 10.70 |
| 30 | 31.706 | 0.4260 | 13.37 |
| 20 | 38.855 | 0.3922 | 20.26 |
| 10 | 72.235 | 0.2480 | 18.86 |

process could be pursued as those reviewed by Lu and Law [47], it is outside the scope of the current effort. Figure 12 shows comparisons of flame structure using both approaches with full chemistry compared to solving Eq. (6) using the 8 step reduced mechanism for the 220 μm particle burning in air shown in Fig. 3. Resulting speedup and error between the burn rates for the reduced models are presented in Table 1. All cases are compared to a baseline case using the fully compressible formulation with 50 nodes and using full chemistry. Using the simplified formulation and reaction mechanism results in an order of magnitude reduction in computational effort with little change in flame structure and an incurred 19% error in burn rates. Further savings can be introduced by reducing the number of nodes. For the 10 node case, the burn rates are still computed within a respectable ~20% error but with nearly two orders of magnitude reduction in computational cost. Comparable trends are also observed using different oxidizers and mixtures of oxidizers (not shown).

## 4. Conclusion

A fully compressible, spherically symmetric aluminum particle combustion model is developed to study the transition from diffusion to kinetically controlled burning. Comparison of model predictions to multi-dimensional simulations and experimental data reveals the effectiveness of the model to reproduce the expected burn time dependencies over a range of pressures and oxidizing environments. Comparisons of the model predictions to flame structure and burn times in several different oxidizing environments agree favorably to available data. A detailed analysis

of flame structure reveals the dominant pathways for the transition of diffusion to kinetically controlled burning are a competition between the consumption rate of AlO and diffusion of $Al_2O$ away from the particle surface which is a function of both pressure and diameter. This information is used to develop two simplified modeling descriptions that can be used in system level simulations. The first is an augmented burn rate model for which the effects of finite-rate chemistry are treated as a perturbation to burn rate models assuming a thin flame structure. This approach is used to predict deflagration flame speeds of aluminum dusty gases. Agreement to data and theory is promising and shows evidence of a maximum flame speed versus diameter corresponding to a trade-off between increases in surface area and decreases in burn rates. Since the diffusion to kinetically controlled transition is largely dictated by the presence of AlO near the particle surface, it is interesting to consider means to promote AlO consumption near the surface (*e.g.*, a surface catalyst), forcing the particle to burn in a diffusion controlled mode at smaller particle sizes. If such a mechanism could be introduced, the location of maximum flame speed would potentially shift to smaller particles resulting in an overall higher peak flame speed. The second simplified modeling description relies on a reduced mechanism and a quasi-steady formulation of the equations allowing for an efficient implicit formulation. Comparisons of the reduced model to the fully compressible model using full kinetics shows significant savings can be achieved with little loss in accuracy for the prediction of burn rates.

## Acknowledgment

## Appendix A

Kinetic mechanism for aluminum combustion with air, steam and carbon dioxide [6,10].

| Reaction | $A$ ($cm^3$/mol/s) | $\alpha$ | $E_a$ (K) |
|---|---|---|---|
| $Al + O_2 \leftrightarrow AlO + O$ | $9.72 \times 10^{13}$ | 0.0 | 80.5 |
| $AlO + O_2 \leftrightarrow AlO_2 + O$ | $4.62 \times 10^{14}$ | 0.0 | 10008.0 |
| $Al_2O_3 \leftrightarrow Al_2O_3c$ | $3.0 \times 10^{15}$ | 0.0 | 0.0 |
| $Al_2O_3 \leftrightarrow Al_2O_2 + O$ | $3.0 \times 10^{15}$ | 0.0 | 49144.4 |
| $Al_2O_3 \leftrightarrow AlO_2 + AlO$ | $3.0 \times 10^{15}$ | 0.0 | 63915.1 |
| $Al_2O_2 \leftrightarrow Al + AlO_2$ | $1.0 \times 10^{15}$ | 0.0 | 74937.1 |
| $Al_2O_2 \leftrightarrow AlO + AlO$ | $1.0 \times 10^{15}$ | 0.0 | 59335.7 |
| $Al_2O_2 \leftrightarrow Al_2O + O$ | $1.0 \times 10^{15}$ | 0.0 | 52466.0 |
| $AlO_2 \leftrightarrow AlO + O$ | $1.0 \times 10^{15}$ | 0.0 | 44564.6 |
| $Al_2O \leftrightarrow AlO + Al$ | $1.0 \times 10^{15}$ | 0.0 | 67035.7 |
| $Al + O + M \leftrightarrow AlO + M$ $H_2/2.8/O_2/1.1/H_2O/1.1/$ $CO_2/4.3/CO/2.1/$ | $3.0 \times 10^{17}$ | −1.0 | 0.0 |
| $O_2 + M \leftrightarrow O + O + M$ | $1.2 \times 10^{14}$ | 0.0 | 54244.0 |
| $Al + H_2O \leftrightarrow H + AlOH$ | $1.14 \times 10^{12}$ | 0.0 | 442.88 |
| $Al + H_2O \leftrightarrow AlO + H_2$ | $9.6 \times 10^{13}$ | 0.0 | 2868.64 |
| $H_2 + M \leftrightarrow H + H + M$ | $2.23 \times 10^{14}$ | 0.0 | 48350.0 |
| $AlH_3 + H \leftrightarrow AlH_2 + H_2$ | $4.75 \times 10^9$ | 1.5 | 0.0 |
| $AlH_3(+M) \leftrightarrow AlH + H_2(+M)$ $LOW/1.01 \times 10^{15}$ 0.0 27089.0/ $TROE/0.06$ 885.0 552.0 3807.0/ | $1.48 \times 10^{13}$ | 0.0 | 30758.9 |
| $Al + H + M \leftrightarrow AlH + M$ | $1.6 \times 10^{17}$ | −0.34 | 0.0 |

**Appendix A** (*continued*)

| Reaction | $A$ ($cm^3$/mol/s) | $\alpha$ | $E_a$ (K) |
|---|---|---|---|
| $AlH + H \leftrightarrow Al + H_2$ | $1.0 \times 10^{13}$ | 0.0 | 0.0 |
| $AlH_2 + H \leftrightarrow AlH + H_2$ | $2.0 \times 10^{13}$ | 0.0 | 0.0 |
| $AlH_2(+M) \leftrightarrow AlH + H(+M)$ $LOW/9.68 \times 10^{14}$ 0.0 19962.0/ $TROE/5.1$ 21.6 493.0 942.0/ | $2.23 \times 10^{14}$ | 0.0 | 48350.0 |
| $Al + CO_2 \leftrightarrow AlO + CO$ | $1.74 \times 10^{14}$ | 0.0 | 3221.4 |
| $AlO + CO_2 \leftrightarrow AlO_2 + CO$ | $1.5 \times 10^{10}$ | 0.0 | −400.1 |
| $H + O + M \leftrightarrow OH + M$ | $6.2 \times 10^{16}$ | −0.6 | 0.0 |
| $H + O_2 \leftrightarrow OH + O$ | $1.59 \times 10^{17}$ | −0.927 | 8492.7 |
| $H_2 + O \leftrightarrow OH + H$ | $3.87 \times 10^4$ | 2.7 | 3151.8 |
| $H_2 + OH \leftrightarrow H_2O + H$ | $2.16 \times 10^8$ | 1.51 | 1732.3 |
| $OH + OH \leftrightarrow H_2O+)$ | $2.10 \times 10^8$ | 1.4 | −199.7 |
| $H + O_2 + M \leftrightarrow HO_2 + M$ | $7.0 \times 10^{17}$ | −0.8 | 0.0 |
| $HO_2 + H \leftrightarrow OH + OH$ | $1.5 \times 10^{14}$ | 0.0 | 505.2 |
| $HO_2 + H \leftrightarrow H_2 + O_2$ | $2.5 \times 10^{13}$ | 0.0 | 348.8 |
| $HO_2 + H \leftrightarrow H_2O + O$ | $5.0 \times 10^{12}$ | 0.0 | 709.6 |
| $HO_2 + O \leftrightarrow O_2 + OH$ | $2.0 \times 10^{13}$ | 0.0 | 0.0 |
| $HO_2 + OH \leftrightarrow H_2O + O_2$ | $6.02 \times 10^{13}$ | 0.0 | 0.0 |
| $HO_2 + HO_2 \leftrightarrow H_2O_2 + O_2$ | $4.2 \times 10^{14}$ | 0.0 | 6030.7 |
| $H_2O_2 + H \leftrightarrow HO_2 + H_2$ | $1.7 \times 10^{12}$ | 0.0 | 1888.7 |
| $H_2O_2 + H \leftrightarrow H_2O + OH$ | $1.0 \times 10^{13}$ | 0.0 | 1804.4 |
| $H_2O_2 + O \leftrightarrow HO_2 + OH$ | $2.8 \times 10^{13}$ | 0.0 | 3223.9 |
| $H_2O_2 + OH \leftrightarrow H_2O + HO_2$ | $7.0 \times 10^{12}$ | 0.0 | 721.7 |
| $AlOH \leftrightarrow AlO + H$ | $1.0 \times 10^{15}$ | 0.0 | 57731.2 |
| $AlOH \leftrightarrow Al + OH$ | $1.0 \times 10^{15}$ | 0.0 | 66438.3 |
| $H + OH + M \leftrightarrow H_2O + M$ $H_2/1.9/O_2/2.6/H_2O/9.5/$ $CO/2.6/CO_2/2.6/$ | $8.4 \times 10^{21}$ | −2.0 | 0.0 |
| $H_2O_2 + M \leftrightarrow OH + OH + M$ $H_2/2.9/O_2/1.2/H_2O/18.5/$ $CO/2.1/CO_2/4.3/$ | $1.0 \times 10^{17}$ | 0.0 | 22856.4 |
| $CO_2(+M) \leftrightarrow CO + O(+M)$ $LOW/5.1 \times 10^{14}$ 0.0 55561.0/ | $9.0 \times 10^{12}$ | 0.0 | 65280.3 |
| $CO + O_2 \leftrightarrow CO_2 + O$ | $2.53 \times 10^{12}$ | 0.0 | 24003.5 |
| $CO + OH(+M) \leftrightarrow CO_2 + H(+M)$ $LOW/1.17 \times 10^7$ 1.35 − 360.8/ | $2.45 \times 10^{-3}$ | 3.68 | −625.5 |
| $CO + HO_2 \leftrightarrow CO_2 + OH$ | $6.40 \times 10^9$ | 0.0 | 11873.3 |

## References

[1] M.K. King, Proc. Combust. Inst. 32 (2009) 2107–2114.
[2] S.R. Turns, S.C. Wong, E. Ryba, Combust. Sci. Technol. 54 (1987) 299–318.
[3] Y. Gan, L. Qiao, Combust. Flame 158 (2) (2011) 354–368. <http://www.sciencedirect.com/science/article/pii/S0010218010002488>.
[4] T. Bazyn, H. Krier, N. Glumac, Proc. Combust. Inst. 31 (2007) 2021–2028.
[5] Y. Huang, G.A. Risha, V. Yang, R.A. Yetter, Combust. Flame 156 (1) (2009) 5–13. <http://www.sciencedirect.com/science/article/pii/S0010218008002861>.
[6] E.B. Washburn, J.A. Webb, M.W. Beckstead, Combust. Flame 157 (2010) 540–545.
[7] S. Mohan, L. Furet, E.L. Dreizin, Combust. Flame 157 (7) (2010) 1356–1363. <http://www.sciencedirect.com/science/article/pii/S0010218009003368>.
[8] P. Lynch, H. Krier, N. Glumac, Proc. Combust. Inst. 32 (2) (2009) 1887–1893. <http://www.sciencedirect.com/science/article/pii/S1540748908002514>.
[9] C. Badiola, R.J. Gill, E.L. Dreizin, Combust. Flame 158 (10) (2011) 2064–2070. <http://www.sciencedirect.com/science/article/pii/S0010218011000939>.
[10] E.B. Washburn, J.N. Trivedi, L. Catoire, M. Beckstead, Combust. Sci. Technol. 108 (8) (2008) 1502–1517.
[11] T. Bazyn, H. Krier, N. Glumac, J. Propul. Power 21 (2005) 577–582.

[12] M.W. Beckstead, A summary of aluminum combustion, Tech. Rep. RTO-EN-023, NATO Research And Technology Organisation, January 2004.

[13] L. Catoire, J. Franatilde, L. Legendre, M. Giraud, J. Propul. Power 19 (2) (2003) 196–202. http://dx.doi.org/10.2514/2.6118.

[14] R.A. Yetter, F. Dryer, Microgravity Combustion: Fire in Free Fall, Academic Press, 2001. pp. 419–478.

[15] A. Makino, C.K. Law, in: Twenty-first Symposium (Int.) on Combustion, The Combustion Institute, 1986, pp. 183–191.

[16] A. Makino, Combust. Flame 90 (1992) 143–154.

[17] M. Beckstead, Combust. Explo. Shock Waves 41 (5) (2005) 533–546.

[18] R.J. Gill, C. Badiola, E.L. Dreizin, Combust. Flame 157 (2010) 2015–2023.

[19] S. Gallier, F. Sibe, O. Orlandi, Proc. Combust. Inst. 33 (2011) 1949–1956.

[20] P. Bucher, R.A. Yetter, F.L. Dryer, E.P. Vicenzi, T.P. Parr, D.M. Hanson-Parr, Combust. Flame 117 (1999) 351–361.

[21] S. Mathur, P. Tondon, S. Saxena, Mol. Phys. 12 (1967) 569.

[22] R. Bird, W. Stewart, E. Lightfoot, Transport Phenomena, John Wiley and Sons, 1960.

[23] A.M. Starik, P.S. Kuleshov, A.S. Sharipov, N.S. Titova, C.-J. Tsai, Combust. Flame 161 (6) (2014) 1659–1667. <http://www.sciencedirect.com/science/article/pii/S0010218013004550>.

[24] P. DesJardin, J.D. Felske, M.D. Carrara, J. Propul. Power 21 (1) (2005) 1–8.

[25] V.A. Babuk, V. Vasilyev, Model of aluminum agglomerate evolution in combustion products of solid rocket propellant, J. Propul. Power 18 (4) (2002) 814–823.

[26] R. Hultgren, P.D. Desai, D.T. Hawkins, M. Gleiser, K.K. Kelley, Selected Values of the Thermodynamics Properties of the Elements, American Society for Metals, 1973.

[27] M.-S. Liou, J. Comput. Phys. 214 (1) (2006) 137–170.

[28] Y. Li, J. Comput. Phys. 133 (1997) 235–255.

[29] J.A. Sethian, S.J. Osher, The design of algorithms for hypersurfaces moving with curvature-dependent speed, Numer. Fluid Mech. 24 (1989).

[30] S.R. Desai, H. Wu, C.M. Rohlfing, L.-S. Wang, J. Chem. Phys. 106 (4) (1997) 1309–1317. <http://link.aip.org/link/?JCP/106/1309/1>.

[31] M.T. Swihart, L. Catoire, Combust. Flame 121 (1–2) (2000) 210–222. <http://www.sciencedirect.com/science/article/pii/S0010218099001285>.

[32] P. Lynch, H. Krier, N. Glumac, Combust. Flame 159 (2012) 793–801.

[33] A. Ermoline, D. Yildiz, E.L. Dreizin, Combust. Flame 160 (12) (2013) 2982–2989. <http://www.sciencedirect.com/science/article/pii/S0010218013002435>.

[34] S. Dushman, J. Lafferty, Scientific Foundations of Vacuum Technique, second ed., Wiley, New York, 1962.

[35] P. Bucher, R.A. Yetter, F.L. Dryer, T.P. Parr, D.M. Hanson-Parr, E.P. Vicenzi, Flame structure measurement of single, isolated aluminum particles burning in air, 1996.

[36] V. Sarou-Kanian, J. Rifflet, F. Millot, I. Gökalp, Combust. Flame 145 (1–2) (2006) 220–230. <http://www.sciencedirect.com/science/article/pii/S0010218005003275>.

[37] K.P. Ruggirello, P. DesJardin, M.R. Baer, E.S. Hertel, Combust. Theory Model. 14 (2010) 41–67.

[38] K.P. Ruggirello, P.E. DesJardin, M.R. Baer, M.J. Kaneshige, E.S. Hertel, Int. J. Multiphase Flow 42 (2012) 128–151. <http://www.sciencedirect.com/science/article/pii/S030193221200033X>.

[39] L.V. Boichuk, V.G. Shevchuk, A.I. Shvets, Combust. Explo. Shock Waves 38 (6) (2002) 651–654.

[40] S. Goroshin, I. Fomenko, J.H.S. Lee, Burning velocities in fuel-rich aluminum dust clouds, in: Symposium (International) on Combustion, vol. 26(2), 1996, pp. 1961–1967. <http://www.sciencedirect.com/science/article/pii/S0082078496800191>

[41] S. Goroshin, M. Bidabadi, J.H.S. Lee, Combust. Flame 105 (1–2) (1996) 147–160. <http://www.sciencedirect.com/science/article/pii/0010218095001832>.

[42] D.R. Ballal, Proc. Roy. Soc. Lond. Ser. A, Math. Phys. Sci. 385 (1788) (1983) 21–51. <http://www.jstor.org/stable/2397471>.

[43] H. Cassel, Reports of Investigations 6551, U.S. Dept. Interior Bureau of Mines.

[44] S.R. Turns, An Introduction to Combustion, McGraw-Hill, Inc., New York, NY, 1996.

[45] F.A. Williams, Combustion Theory, The Benjamin/Cummings Publishing Company, Menlo Park, CA, 1985.

[46] C.K. Law, Combustion Physics, Cambridge University Press, 2006.

[47] T. Lu, C.K. Law, Prog. Energy Combust. Sci. 35 (2) (2009) 192–215. <http://www.sciencedirect.com/science/article/pii/S036012850800066X>.

[48] I. Glassman, Combustion, Academic Press, New York, NY, 1996.